## **Green Chemistry**



PAPER View Article Online
View Journal | View Issue



**Cite this:** *Green Chem.*, 2020, **22**, 7491

Received 27th July 2020, Accepted 9th October 2020 DOI: 10.1039/d0gc02580a

rsc.li/greenchem

# $Li_xSiON$ (x = 2, 4, 6): a novel solid electrolyte system derived from agricultural waste†‡

Xinyu Zhang, Eleni Temeche and Richard M. Laine 🕩 \*

A set of Li<sub>x</sub>SiON (x = 2, 4, 6) polymer precursors to a novel solid-state electrolyte system were synthesized starting from rice hull ash (RHA), an agricultural waste, providing a green route towards the assembly of all solid-state batteries (ASSBs). Silica, ~90 wt% in RHA, can be catalytically (alkali base) dissolved (20–40 wt%) in hexylene glycol (HG) and distilled directly from the reaction mixture as the spirosiloxane  $[(C_6H_{14}O_2)_2Si, SP]$  at 200 °C. SP can be lithiated using controlled amounts of LiNH<sub>2</sub> to produce Li<sub>x</sub>SiON oligomers/polymers with MWs up to ~1.5 kDa as characterized by FTIR, MALDI-ToF, multinuclear NMR, TGA-DTA, XRD, XPS, SEM and EDX. XPS analyses show that Li contents depend solely on added LiNH<sub>2</sub> but found N contents are only  $\leq 1$  at%. NH<sub>2</sub> likely is removed as NH<sub>3</sub> during sample preparation (vacuum/overnight). In contrast, MALDI indicates N contents of ~5–30 at% N with shorter drying times (vacuum/minutes). The NMR positive chemical shifts suggest that precursor bound Li<sup>+</sup> ions dissociate easily, beneficial for electrochemical applications. The Li<sub>6</sub>SiON precursor show fluxional behavior implying high Li<sup>+</sup> mobility. Dense microstructures are observed for Li<sub>4</sub>SiON and Li<sub>6</sub>SiON pellets heated to 200 °C/2 h/N<sub>2</sub>. Impedance studies suggest that ionic conductivities increase with Li content; the Li<sub>6</sub>SiON precursor offers the highest ambient conductivity of  $8.5 \times 10^{-6}$  S cm<sup>-1</sup> after heating to 200 °C/2 h/N<sub>2</sub>.

#### 1. Introduction

To reduce the consumption of traditional energy sources, i.e., fossil fuels, and emission of greenhouse gases, researchers have long sought to replace combustion-based energy technologies. Electrochemical energy storage/conversion systems, including lithium-ion batteries (LIBs) have become subjects of great interest. 1-3 LIBs are now used intensely in applications ranging from simple replacements for traditional batteries in toys, medical devices, and portable electronics. Although, LIBs are instrumental in the commercialization of electric vehicles; the use of organic solvent based liquid electrolytes with inadequate electrochemical and thermal stabilities introduces inherent safety risks and restrains operating temperatures.<sup>4-7</sup> Non-flammable, solid-state electrolytes offer an escape from such problems offering potential for both wider operating temperatures coincident with higher energy-densities. 4-6,8 The potential to formulate solid-state electrolytes from agricultural waste (e.g. rice hull ash, RHA) therefore offers two exciting

Dept. of Materials Science and Engineering, University of Michigan, Ann Arbor, MI 48109-2136, USA. E-mail: talsdad@umich.edu

opportunities. One is to valorize the waste of a commodity product (RHA) and the potential to coincidentally reduce the carbon footprint of extensively used battery materials. This then is the motivation for work reported here.

Li<sup>+</sup>-containing oxynitride amorphous thin films are promising materials for electrochemical applications as solid electrolytes due to their high ionic conductivity, mechanical stability and chemical durability. Most studies focus on lithium phosphorous oxynitride (LiPON) thin films as suggested by the extensive literature on this topic.<sup>9–35</sup> There are a few reports on borate analogs, lithium boron oxynitrides (LiBON).<sup>36–39</sup> However, the ionic conductivity (at ambient) for LiBON (10<sup>–8</sup> S cm<sup>–1</sup>) is much lower than LiPON (10<sup>–6</sup> S cm<sup>–1</sup>).<sup>9–12</sup> Studies on other Li-containing oxynitrides are also reported including lithium sulfur oxynitride (LiSON) with ambient conductivities of 10<sup>–6</sup>–10<sup>–5</sup> S cm<sup>–1</sup>,<sup>40,41</sup> and lithium vanadium oxynitride (LiVON) with conductivities of 10<sup>–4</sup>–10<sup>–5</sup> S cm<sup>–1</sup> at 330 °C.<sup>42,43</sup>

A number of research groups have explored silicon oxynitride MSiON (M = Li, Na) glass-ceramics with respect to their crystallization and bonding arrangements,  $^{44-48}$  mechanical properties,  $^{44,47}$  chemical durability and conductivities. Typically, such glasses are prepared by melt mixing Li<sub>2</sub>O or Na<sub>2</sub>O, SiO<sub>2</sub> and Si<sub>3</sub>N<sub>4</sub> at 1400–1500 °C/1–3 h in BN crucibles under N<sub>2</sub>.  $^{45,46,48-50}$  The conductivity for MSiON is attributed to alkali ion transport, which increases with increasing N content.  $^{49,50}$  The literature explanation for this behavior

<sup>†</sup>This paper is dedicated to the memory of Prof. Dr. Andreas Hintennach, deceased May 10, 2020, a friend and mentor.

<sup>‡</sup>Electronic supplementary information (ESI) available. See DOI: 10.1039/d0gc02580a

suggests that Si–N bonds are more covalent (less ionic) than Si–O bonds, the electrostatic force exerted on alkali ions decreases on nitridation resulting in reduced activation energy.  $^{44-50}$  A similar N for O effect is found for LiPON glasses.  $^{13-18}$  However, the ambient conductivities of M–Si–O–N glasses remain at  $10^{-8}$ – $10^{-7}$  S cm $^{-1}$ .

A doctoral thesis by Jarkaneh<sup>43</sup> describes novel Li<sup>+</sup> oxynitride conductors including Li<sub>3+x</sub>PO<sub>4-x</sub>N<sub>x</sub>, Li<sub>3+x</sub>VO<sub>4-x</sub>N<sub>x</sub>, Li<sub>2+y</sub>ZnSiO<sub>4-y</sub>N<sub>y</sub> and Li<sub>2+y</sub>MgSiO<sub>4-y</sub>N<sub>y</sub> solid solutions. N-Doping of all compositions generates a  $\gamma$ -phase, except in Li<sub>3</sub>VO<sub>4</sub> which generates a  $\beta$ -phase. The  $\gamma$ -phase structures are typical for Li<sup>+</sup> superionic conductors (LISICON), where cations are tetrahedrally coordinated.

As shown in Table S1,‡ N-doping improves conductivities by up to two orders of magnitude in N-doped  $\mathrm{Li_3(P,V)O_4}$  and 4–6 orders in N-doped  $\mathrm{Li_2(Zn,Mg)SiO_4}$ . The activation energy decreases by about 0.3 eV in N-doped  $\mathrm{Li_3(P,V)O_4}$  and 0.6–0.7 eV in N-doped  $\mathrm{Li_2(Zn,Mg)SiO_4}$ . Higher ionic conductivities and lower activation energies in N-doped samples are attributed to higher numbers of interstitial  $\mathrm{Li^+}$  created as a result of substitution of N for O. Therefore, it is reasonable to envision that

 ${\rm Li_4SiO_4.^{60-64}}$  For the binary system, compositions with 40–60 mol%  ${\rm Li_4SiO_4}$  typically give the highest ionic conductivities of ~10<sup>-6</sup> S cm<sup>-1</sup> at 20 °C. <sup>55,57–59</sup> For the ternary system, the composition  $(1-z)[0.6{\rm Li_2S}-0.4{\rm SiS_2}]-z{\rm Li_4SiO_4}$  (z=0–10 mol%) exhibits a room temperature conductivity of  $10^{-4}$ – $10^{-3}$  S cm<sup>-1</sup>. <sup>60–63</sup>

The above studies suggest that  $\text{Li}_4\text{SiO}_4$  is a reasonable candidate for solid electrolyte applications. However, to the best of our knowledge, there have been no reports on N-doped  $\text{Li}_4\text{SiO}_4$  (or  $\text{Li}_x\text{SiON}$ ) as solid electrolytes. Given our previous success in developing polymer precursor derived  $\text{Li}_x\text{PON-like}$  electrolytes, <sup>65–67</sup> we present here a novel and green approach to  $\text{Li}_x\text{SiON}$  oligomer/polymer precursors (x = Li/Si mole ratio).

Recently, we reported processing "green" hybrid Li<sup>+</sup> capacitor (LIC) electrodes using the plentiful agricultural waste, RHA, as the starting material. <sup>68</sup> The basis for this report was the use of silica depleted RHA (SDRHA,  $\approx$ 65 wt% SiO<sub>2</sub>, 35 wt% C); a carbon/silica nanocomposite. This nanocomposite derives from SiO<sub>2</sub> extraction from RHA by simple distillation of the spirosiloxane [( $C_6H_{14}O_2$ )<sub>2</sub>Si, SP] at 200 °C, as illustrated in reaction (1):

N-doping of other  $\gamma$ -structured materials, including Li<sub>4</sub>SiO<sub>4</sub>, can be expected to improve ionic conductivity.

Indeed, studies show that  $\text{Li}_4\text{SiO}_4$  may offer utility as a solid electrolyte. Wu *et al.*<sup>51,52</sup> synthesized  $\text{Li}_4\text{SiO}_4$  powders (particle sizes  $\approx 100$  nm) *via* sol–gel processing using  $\text{SiO}_2$  (aerosil) and  $\text{LiOH}\cdot\text{H}_2\text{O}$  as the starting materials and citric acid ( $\text{C}_6\text{H}_8\text{O}_7\cdot\text{H}_2\text{O}$ ) as the chelating agent.  $\text{Li}_4\text{SiO}_4$  pellets (diameter

We report here that this spirosiloxane "byproduct" provides the starting point for a series of Li<sup>+</sup> conducting polymer precursors on reaction with LiNH<sub>2</sub>, generically illustrated by reaction (2). Such a synthetic approach provides environmental advantages including green source, low cost, low temperature, low energy consumption, emission-free, and scalable features.

= 10 mm, thickness = 2 mm) sintered at 1000 °C/4 h exhibited bulk conductivities of  $\sim 10^{-3}$  S cm<sup>-1</sup> at 400 °C. Similarly, Adnan *et al.*<sup>53</sup> prepared Li<sub>4</sub>SiO<sub>4</sub> powders by sol–gel, then pelletized and sintered at 600–750 °C/4 h finding a bulk conductivity of  $\sim 3 \times 10^{-6}$  S cm<sup>-1</sup> at ambient, suggesting potential use as LISICON structured solid electrolytes for low-temperature applications.

Furthermore, various studies have described  $\text{Li}_4\text{SiO}_4$ -based solid electrolytes, including the binary and ternary systems:  $\text{Li}_4\text{SiO}_4$ - $\text{Li}_3\text{XO}_4$  (X = V, As, P, etc.),  $^{54-59}$  and  $\text{Li}_2\text{S-SiS}_2$ -

## 2. Experimental section

#### 2.1. Materials

RHA was provided by Wadham Energy LP (Williams, CA); it was milled in dilute hydrochloric acid (HCl) to remove impurities prior to use. The solvent and reactants, 2-methyl-2,4-pentanediol (hexylene glycol, HG) and lithium amide (LiNH<sub>2</sub>) were purchased from Acros Organics. Sodium hydroxide (NaOH), HCl and tetrahydrofuran (THF) were purchased from Sigma-Aldrich. Hexane was purchased from Fisher Chemical,

and ethanol was provided by Decon Labs, Inc. THF was distilled from sodium benzophenone ketyl under nitrogen prior to use. All other chemicals were used as received.

#### 2.2. Synthesis of spirosiloxane

Silica from RHA can be reacted with HG using catalytic base forming SP at 200 °C,<sup>70,71</sup> which distills directly out of the reaction mixture per eqn (1).

Typical spirosiloxane synthesis. To a dry 500 mL round-bottom flask are added 300 mL HG (excess amount) and NaOH (3.0 g, 75 mmol). The solution is heated to 200 °C/3 h with stirring to remove water, then dried RHA ( $\sim$ 50 g,  $\sim$ 90 wt% silica content) is added. After 100 mL HG distills off, another 100 mL HG is added until 500 mL HG has reacted and/or distilled out as a mixture of SP, H<sub>2</sub>O and HG during silica depolymerization.

The distilled mixture of SP,  $\rm H_2O$  and HG (500 mL) is washed with hexane (500 mL) and water (3 × 250 mL). HG is soluble in water, but SP is not. Then the hexane layer (containing SP) is dried over magnesium sulfate and collected. In the final step, the hexane is removed on a rotary evaporator to yield 37 g of the SP product (~70% yield). The SP can be further purified by redistillation. The product is dried at 60 °C/12 h/vacuum.

The remaining SDRHA is filtered off. Fig. S1‡ compares the TGA-DTAs of RHA before and after reaction, *i.e.*, RHA and SDRHA, which show silica contents of 88 and 64 wt% respectively (ceramic yield or CY at 800  $^{\circ}$ C), suggesting ~27 wt% silica dissolution.

#### 2.3. Syntheses of $Li_x$ SiON precursors

 $\text{Li}_x \text{SiON}$  precursors are synthesized by reacting SP with  $\text{LiNH}_2$  (mole ratio of  $\text{LiNH}_2/\text{SP} = x$ ), as suggested in eqn (2). In theory, one SP molecule can be envisioned to offer two coordination sites for  $\text{LiNH}_2$  ( $\text{Li}_2 \text{SiON}$ ),  $^{72}$  but below our studies suggest that excess  $\text{LiNH}_2$  can react with SP forming  $\text{Li}_4 \text{SiON}$  and  $\text{Li}_6 \text{SiON}$  precursors likely by partial displacement of one or more Si-O bonds.

Example of Li<sub>6</sub>SiON synthesis. In a 200 mL round bottom Schlenk flask equipped with a reflux condenser, SP (3.9 g, 15.0 mmol) and LiNH<sub>2</sub> (2.2 g, 95.8 mmol) are added to ~80 mL distilled THF under N<sub>2</sub>. The reaction is kept running at 60 °C/2 weeks (w)/N<sub>2</sub>. Initially, the reaction is a cloudy white mixture that turns darker over time. After running at 60 °C/2 weeks, the reaction mixture becomes a brown solution (Fig. S2 $^+_{+}$ ).

To obtain the yield, the reaction mixture is allowed to settle for 1 h, a small sample (5 mL) is taken from the top of the mixture to a 25 mL Schlenk flask, and vacuum dried at 60 °C/1 h. The product is a 0.37 g orange solid indicating a total yield for the solution of  $\sim$ 6 g; slightly lower than the mass sum of the starting materials (6.1 g) suggesting the product is almost fully soluble and stable in THF. Table 1 records the LiNH<sub>2</sub> quantities used for different precursors. Fig. S3‡ shows optical images of representative Li<sub>x</sub>SiON precursor powders

Table 1 Syntheses of Li<sub>x</sub>SiON precursors

Precursor	LiNH <sub>2</sub> /SP <sup>a</sup>	Appearance <sup>b</sup>
Li <sub>2</sub> SiON	2.1-2.2	Orange/light-brown solution
Li <sub>4</sub> SiON Li <sub>6</sub> SiON	4.2-4.4 6.4-6.6	Orange/light-brown solution Brown solution

 $<sup>^</sup>a$  Typically, a 5–10 mol% excess LiNH  $_2$  is added.  $^b$  The appearances of precursor THF solutions (Fig. S2‡).

dried at 60 °C/1 h/vacuum and pellets pelletized hydraulically at 10 ksi/20 s with a 13 mm diameter die.

#### 3. Results and discussion

Our objectives in this work were first to carefully verify that the prepared precursors contain nitrogen and form oligomers as the first step in exploring their utility as  $\text{Li}_x \text{SiON}$  precursors. Once having demonstrated well-defined compositions, the next step was to explore their properties as electrolytes. For clarity and simplicity, the precursors are simply labeled as  $\text{Li}_x \text{SiON}$  (x = 2, 4, 6) rather than including a complete chemical formula for reasons that become apparent below.

The apparent structures and chemical compositions of  $\text{Li}_x \text{SiON}$  precursors were analyzed using FTIR, matrix-assisted laser desorption/ionization (MALDI-ToF), multi-nuclear NMR, TGA-DTA, XRD, X-ray photoelectron spectroscopy (XPS), scanning electron microscopy (SEM) and energy-dispersive X-ray spectroscopy (EDX). The results of these analyses are presented just below followed by electrochemical impedance spectroscopy (EIS) characterization.

#### 3.1. Characterization of LixSiON precursors

Fig. 1a shows representative FTIRs of  $\text{Li}_x \text{SiON}$  (dried at 60 °C/1 h/vacuum) compared to SP. All precursors show similar SP peaks; in addition, the broad peak at ~3400 cm<sup>-1</sup> is ascribed to  $\nu \text{N-H}$ , with N–H overtones at ~1600 cm<sup>-1</sup>. The  $\text{Li}_4 \text{SiON}$  and  $\text{Li}_6 \text{SiON}$  precursors exhibit a small  $\nu \text{N-H}$  peak at ~3600 cm<sup>-1</sup> evident of residual unreacted LiNH<sub>2</sub> (Fig. S4‡) as excess LiNH<sub>2</sub> was used to synthesize both  $\text{Li}_4 \text{SiON}$  and  $\text{Li}_6 \text{SiON}$  precursors.  $\text{Li}_x \text{SiON}$  precursors dried at temperatures  $\leq 100$  °C show similar FTIRs as illustrated by Fig. 1b, FTIRs of  $\text{Li}_6 \text{SiON}$  dried at RT-100 °C/vacuum. Likewise, as discussed below, very similar XRD patterns are also observed for precursors dried at low temperatures ( $\leq 100$  °C).

Precursor molecular weights (MWs) as well as possible compositions were analyzed using both positive- and negative-ion MALDIs, as done previously for Li<sub>x</sub>PON and Li<sub>x</sub>SiPON precursors. The ion source in the negative-ion mode comes from the precursor itself which loses Li<sup>+</sup>; for the positive-ion mode, the ion source is Ag<sup>+</sup> from AgNO<sub>3</sub> and there is no loss of Li<sup>+</sup>. With the assistance of a Python program (see ESI‡), calculations based on MALDI provide insights into the materials' possible compositions and structures.

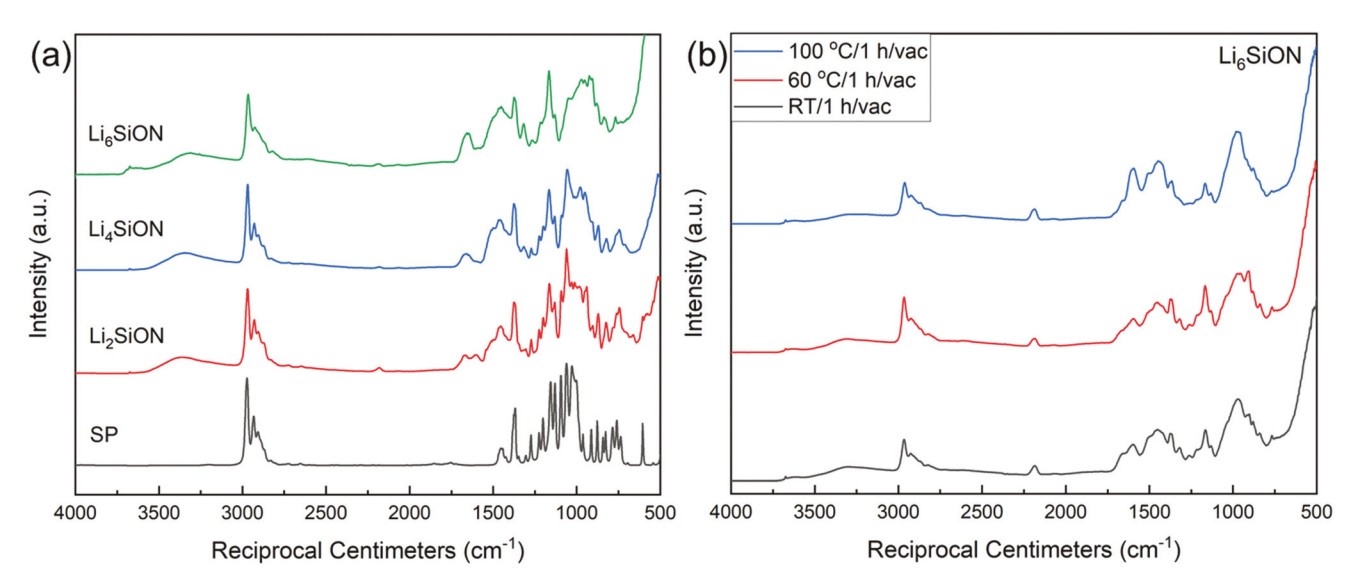


Fig. 1 FTIRs of (a) Li<sub>x</sub>SiON precursors (60 °C/1 h/vacuum) and SP (60 °C/12 h/vacuum), (b) Li<sub>6</sub>SiON dried at RT, 60° and 100 °C/1 h/vacuum.

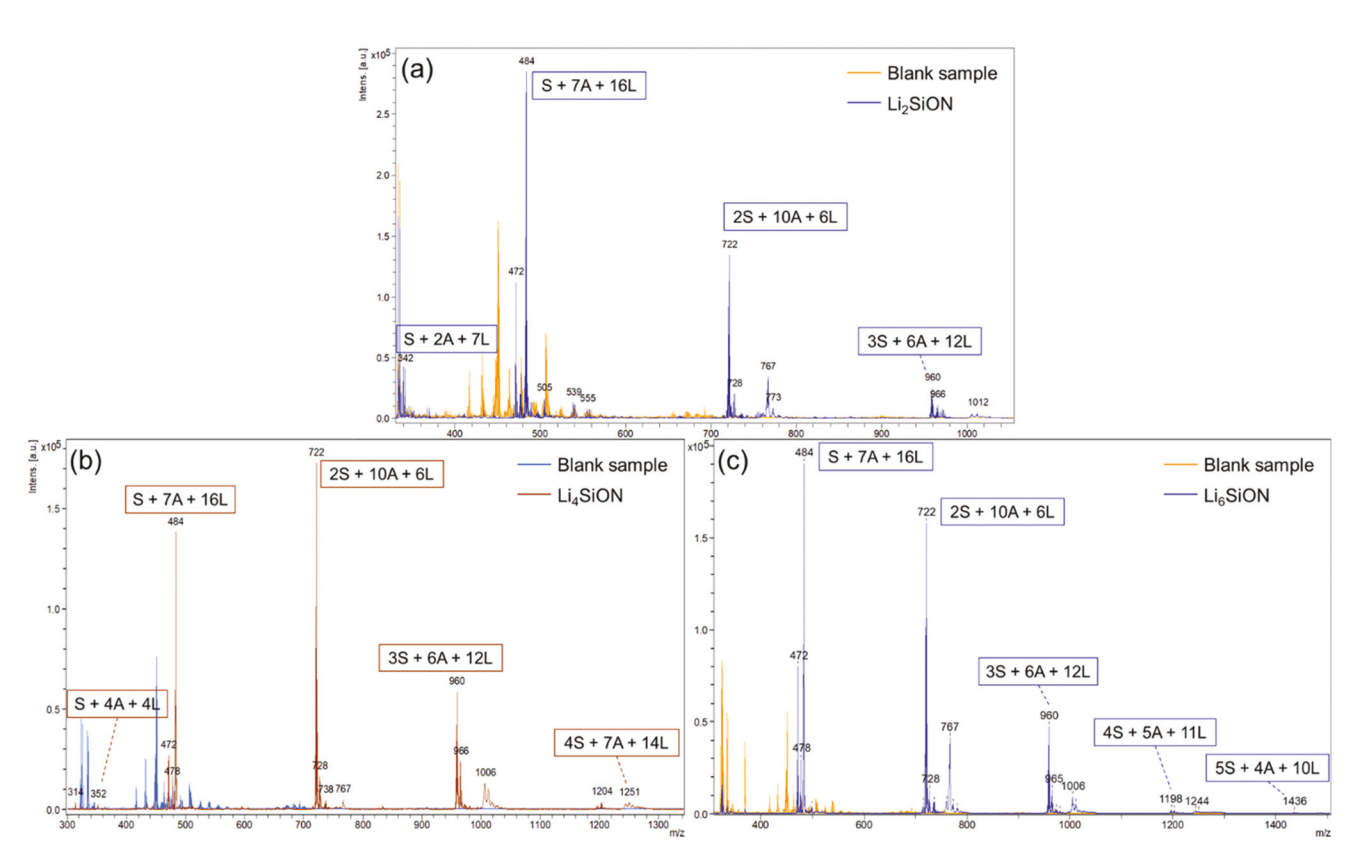


Fig. 2 Positive-ion mode MALDIs of blank vs.  $Li_x$ SiON precursors,  $Li_2$ SiON (a),  $Li_4$ SiON (b) and  $Li_6$ SiON (c), and possible compositions of selected peaks. S = SP,  $A = -NH_2$ ,  $L = Li^+$ .

Fig. 2 shows positive-ion mode MALDIs of Li<sub>x</sub>SiON precursors and possible compositions of selected peaks. Negative-ion mode MALDIs are given in Fig. S5;‡ the complete composition calculations are listed in Table S2.‡ Table 2 records calculated properties of Li<sub>x</sub>SiON precursors derived from MALDI peaks and their intensities.

In general, the  $\text{Li}_x \text{SiON}$  precursors show similar peaks with each peak consisting of different combinations of SP,  $-\text{NH}_2$  and  $\text{Li}^+$ . With higher Li content, the maximum MW (highest m/z) increases; all precursors formed oligomers with SP = 3–5 (Table 2). Composition calculations (Fig. 2 and Table S2‡)

Table 2 Properties of Li<sub>x</sub>SiON precursors derived from MALDI

Precursor	Max. MW $(m/z)^a$	Max. monomer units <sup>b</sup>	N at% <sup>c</sup>	Li at% <sup>c</sup>
Li <sub>2</sub> SiON	1012 (P)	3 (P)	7.7 ± 3.0 (w. H)	8.3 ± 4.6 (w. H)
_	946 (N)	3 (N)	$17.4 \pm 6.7 \text{ (wo. H)}$	$18.2 \pm 8.7$ (wo. H)
Li <sub>4</sub> SiON	1251 (P)	4 (P)	$8.5 \pm 2.8  (w.  H)$	$9.7 \pm 5.1  (w.  H)$
	1002 (N)	3 (N)	$18.9 \pm 6.2$ (wo. H)	$20.9 \pm 9.7$ (wo. H)
Li <sub>6</sub> SiON	1436 (P)	5 (P)	$8.4 \pm 2.9  (w.  H)$	$9.2 \pm 4.7  (w.  H)$
	1196 (N)	4 (N)	$18.6 \pm 6.5 \text{ (wo. H)}$	$21.1 \pm 8.6$ (wo. H)

<sup>&</sup>lt;sup>a</sup> Maximum molecular weights. P = positive-ion mode, N = negative-ion mode. <sup>b</sup> Maximum monomer units = maximum number of SP by calculation. <sup>c</sup> Calculated N/Li atomic percentages. "w. H": including H as part of the calculation; "wo. H" excluding H, providing comparison to XPS studies below.

suggest that there are typically 5–10 –NH<sub>2</sub> groups and 8–13 Li<sup>+</sup> in each precursor structure with only 1–5 SP units, which is much higher than available sites for LiNH<sub>2</sub> [two for each SP, see reaction (2)]. One possible explanation is that some Li<sup>+</sup> containing species exist as clusters in addition to those that interact with SP. It is also possible that ring-opening leads to the formation of more Si–NH bonds and Li–O–HG bonds, NMR data below do not support such hypothesis but in fact also do not disprove the possibility.

A similar pattern is observed for both ion modes: precursors show peaks in separate groups, the difference between every two peaks in each group is typically 7 or 14 Da, which corresponds to one or two Li<sup>+</sup> (7 Da). In some cases, the distance of two peaks is 15–16 Da, which fits better with –NH<sub>2</sub> (16 Da). It is likely that each group of peaks corresponds to a certain structure, and each peak in that group corresponds to different numbers of Li<sup>+</sup> and –NH<sub>2</sub>. The composition calculations listed in Table S2‡ also indicate such a pattern.

Additionally, similar peaks are observed in both positive/negative-ion modes, but the start/end peaks of each group in the positive-ion mode generally shift higher (integer  $\times$  7 m/z = different numbers of Li<sup>+</sup>) as there is no loss of Li<sup>+</sup>.

Atomic percentages (at%) of N and Li calculated from possible compositions (Table S2 $^{+}$ ) are also given in Table 2. Since the composition calculation derived from MALDI gives mathematical combinations and multiple possible results are generated for each peak; for convenience, only one is chosen that may not reflect the true structure. Therefore, the at% calculated from MALDI is meant solely to give a qualitative idea of N contents. As discussed below, XPS and EDX studies were performed to deduce the elemental at% makeup of the Li $_x$ SiON precursors.

The chemical environments and structures for  $\text{Li}_x\text{SiON}$  precursors were further elucidated using NMR. Dried  $\text{Li}_x\text{SiON}$  powders (0.05 g, RT/1 h/vacuum) were dissolved in 1 mL CDCl<sub>3</sub>.

Fig. S6‡ compares the  $^1$ H NMRs of the Li $_x$ SiON precursors (RT/1 h/vacuum), THF and SP. All Li $_x$ SiON precursors show peaks at 3.7 and 1.8 ppm in addition to SP peaks, which are ascribed to residual THF. Unlike Li $_4$ SiON and Li $_2$ SiON precursors, Li $_6$ SiON shows no original SP peaks but a broad peak at 1–1.5 ppm (–CH $_3$ /CH $_2$ ) indicating fluxional behavior.  $^{73,74}$ 

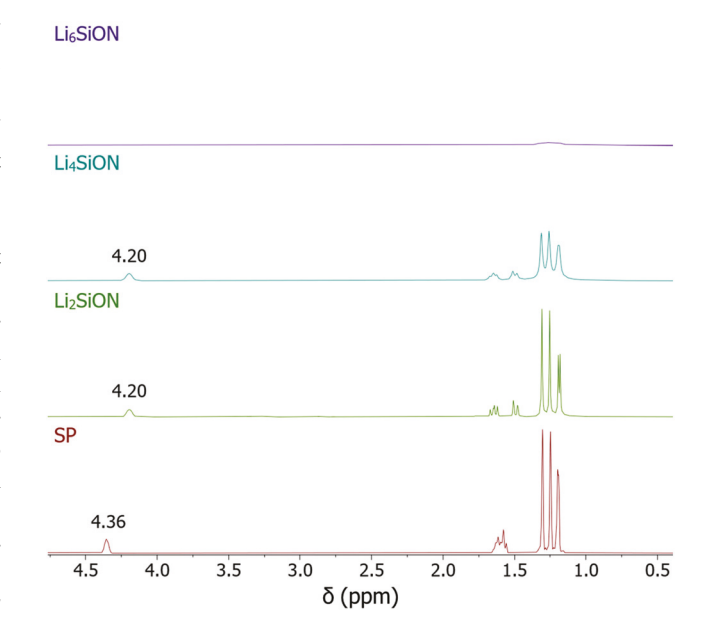


Fig. 3 <sup>1</sup>H NMRs of Li<sub>x</sub>SiON precursors (60 °C/24 h/vacuum) and SP.

To eliminate residual THF,  $\rm Li_xSiON$  precursors were further dried at 60 °C/24 h/vacuum in a vacuum oven. The dried solids (0.05 g each) were added to 1 mL CDCl<sub>3</sub>, respectively. All formed suspensions after stirring overnight/RT, suggesting reduced solubility after prolonged drying.

Fig. 3 compares the  $^{1}$ H NMRs of the Li<sub>x</sub>SiON precursors (60  $^{\circ}$ C/24 h/vacuum) and SP, no THF peaks (3.7 and 1.8 ppm) are observed. Similar to precursors dried at RT/1 h/vacuum (Fig. S6‡), Li<sub>6</sub>SiON (60  $^{\circ}$ C/24 h/vacuum) shows only a small and broad  $^{\circ}$ CH<sub>2</sub> peak at 1.2–1.3 ppm, suggesting fluxional behavior.

Both Li<sub>4</sub>SiON and Li<sub>2</sub>SiON precursors show a peak at 4.2 ppm, likely the -CHO group from SP that shifts due to interaction with Li<sup>+</sup>, suggesting Li<sup>+</sup> interacts more directly with O lone electron pairs from SP. The same -CH<sub>3</sub> peaks from SP are observed in Li<sub>4</sub>SiON and Li<sub>2</sub>SiON precursors, but the intensity is reduced for Li<sub>4</sub>SiON, suggesting there may be partial fluxional behavior for the Li<sub>4</sub>SiON precursor.

Similarly, <sup>13</sup>C NMRs of the Li<sub>x</sub>SiON precursors dried at RT/ 1 h/vacuum exhibit THF peaks at 68.1 and 25.7 ppm (Fig. S7‡),

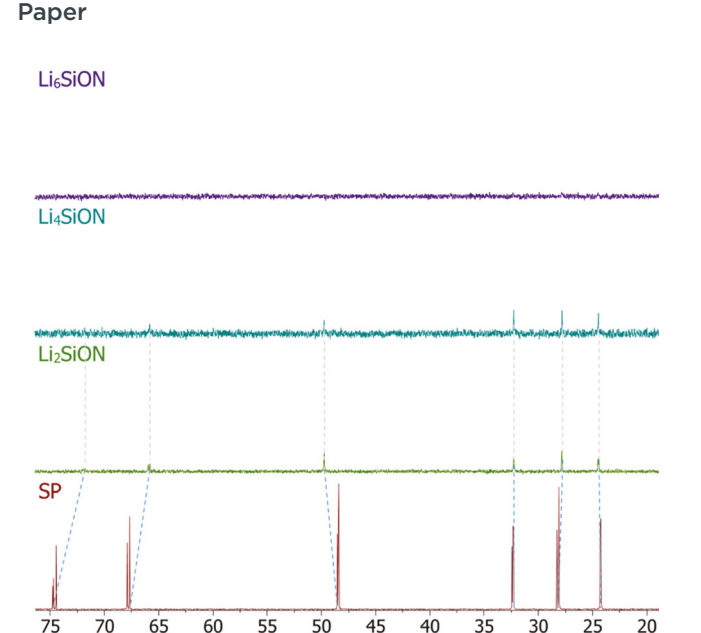


Fig. 4 <sup>13</sup>C NMRs of Li<sub>x</sub>SiON precursors (60 °C/24 h/vacuum) and SP.

δ (ppm)

but no THF peaks are observed for  $\text{Li}_x \text{SiON}$  precursors dried at 60 °C/24 h/vacuum (Fig. 4). Both  $\text{Li}_4 \text{SiON}$  and  $\text{Li}_2 \text{SiON}$  (60 °C/24 h/vacuum) show small SP peaks that shift due to interaction with  $\text{Li}^+$ , and the –CO and –CHO show higher  $\Delta \delta_C$  (qualitative, blue dash lines in Fig. 4) than –CH<sub>2</sub> and –CH<sub>3</sub> peaks, suggesting  $\text{Li}^+$  likely interacts with the O from SP, in agreement with the  $^1 \text{H}$  NMR.

The disappearance of SP peaks for the  $\text{Li}_6\text{SiON}$  precursor (Fig. 4 and S7‡) again reflects fluxional behavior pointing to rapid exchange of  $\text{Li}^+$  in associated clusters. Lee *et al.*<sup>75</sup> studied exchange dynamics in  $\text{Li}^+$  liquid electrolytes of 1.0 M LiPF<sub>6</sub> in DEC and PC/DMC (1:1 vol.). Ultrafast fluxional behavior of  $\text{Li}^+$  carbonate complexes is observed (electrostatic interactions forming and breaking in picoseconds) as proven by coherent 2-D infrared spectroscopy, suggesting macroscopic  $\text{Li}^+$  transport may be related to microscopic fluctuation of solvation. We can suggest that fast chemical exchange dynamics will also play an important role in solvation and de-solvation of  $\text{Li}^+$  in solid polymer electrolytes.

Fig. 5 compares the  $^{7}\text{Li}$  NMRs of Li $_{x}$ SiON precursors (RT/1 h/vacuum), the  $\delta_{\text{Li}}$  shifts downfield with increasing Li content, especially for the Li $_{6}$ SiON precursor suggesting Li $^{+}$  ions are well solvated. The excess Li $^{+}$  likely forms clusters in agreement with the work of See *et al.*  $^{76}$  where  $\delta_{\text{Li}}$  shifts to higher frequencies as Li $^{+}$  concentration increases (LiTFSI in DOL/DME), as also found in our previous studies on Li $_{x}$ PON-like polymer precursors.  $^{65}$  These results suggest the downfield shift is due to deshielding of Li $^{+}$  (reduced electron density around Li $^{+}$ ), *i.e.*, increased numbers of Li $^{+}$  interacting with one SP molecule (coordination numbers change).

However, broad  $^7\text{Li}$  bands with low intensities centered at  $\sim$ 0 ppm are observed for  $\text{Li}_x\text{SiON}$  precursors dried at 60  $^\circ\text{C}/$ 24 h/vacuum due to low solubility (Fig. S8‡), suggesting that THF aids in dissolution of  $\text{Li}^+$ .

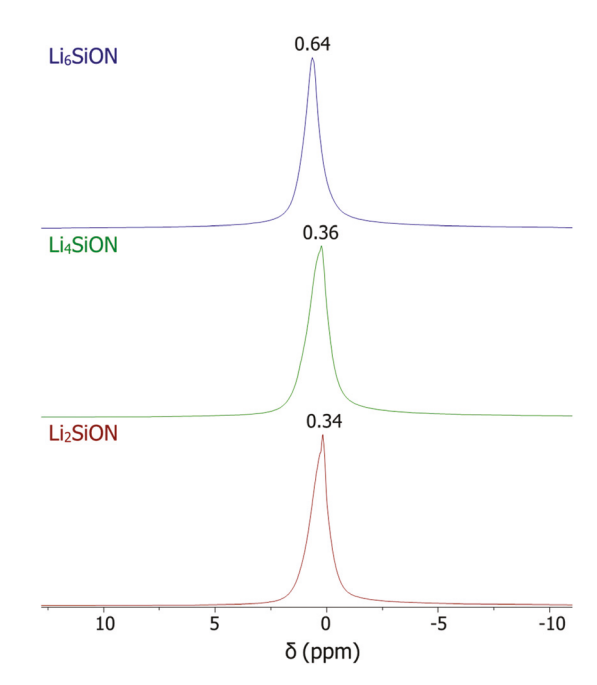


Fig. 5 <sup>7</sup>Li NMRs of Li<sub>x</sub>SiON precursors (RT/1 h/vacuum).

 $^{29} Si$  NMRs of Li $_x SiON$  precursors and SP are presented in Fig. S9.‡ For precursors dried at RT/1 h/vacuum (Fig. S9a‡), similar to  $^1 H$  and  $^{13} C$  studies, no SP peaks were found for the Li $_6 SiON$  precursor, while Li $_2 SiON$  and Li $_4 SiON$  precursors show the same  $\delta_{Si}$  at -81.3 ppm as SP, suggesting no chemical environment change on the O–Si–O bonds for Li $_2 SiON$  and Li $_4 SiON$  precursors, but fluxional behavior for the Li $_6 SiON$  precursor.

However, no <sup>29</sup>Si signals are observed for Li<sub>x</sub>SiON precursors dried at 60 °C/24 h/vacuum (Fig. S9b‡), likely due to reduced solubility, in agreement with <sup>7</sup>Li NMR above.

The thermal stability of  $\text{Li}_x \text{SiON}$  precursors was investigated by TGA-DTA studies. Fig. 6 compares representative TGA-DTAs (800 °C/10 °C min<sup>-1</sup>/N<sub>2</sub>) of  $\text{Li}_x \text{SiON}$  precursors (dried at 60 °C/10 h/vacuum). All precursors typically show 5% mass loss temperatures ( $T_{5\%}$ ) > 100 °C; the major mass loss (from ~100 °C to ~300°–450 °C) is associated with evaporation and/or decomposition of organics. Additionally, the  $\text{Li}_6 \text{SiON}$  precursor exhibits a second mass loss at ~650 °C, associated with excess  $\text{LiNH}_2$  decomposition. To Overall, the CYs (800 °C) of  $\text{Li}_x \text{SiON}$  precursors are  $\text{Li}_6 \text{SiON} > \text{Li}_4 \text{SiON} > \text{Li}_2 \text{SiON}$  in ~10 wt% increments (Fig. 6) correlated with MWs (Fig. 2 and Table 2) and  $\text{Li}_5 \text{Contents}$ .

Unlike the  $\rm Li_x SiON$  precursors, SP evaporates/distills fully at ~100°-200 °C (Fig. S10‡) due to its high vapor pressure. Consequently, added LiNH<sub>2</sub> promotes formation of oligomers/polymers with higher MWs and stable polymer precursors and eventually ceramics form at higher temperatures as demonstrated below.

Fig. S11a‡ compares the XRDs of Li<sub>x</sub>SiON (dried at 60 °C/1 h/vacuum) and SP. SP exhibits various crystalline peaks that are indexed to space group 10: P2/m by Expo2014, while the

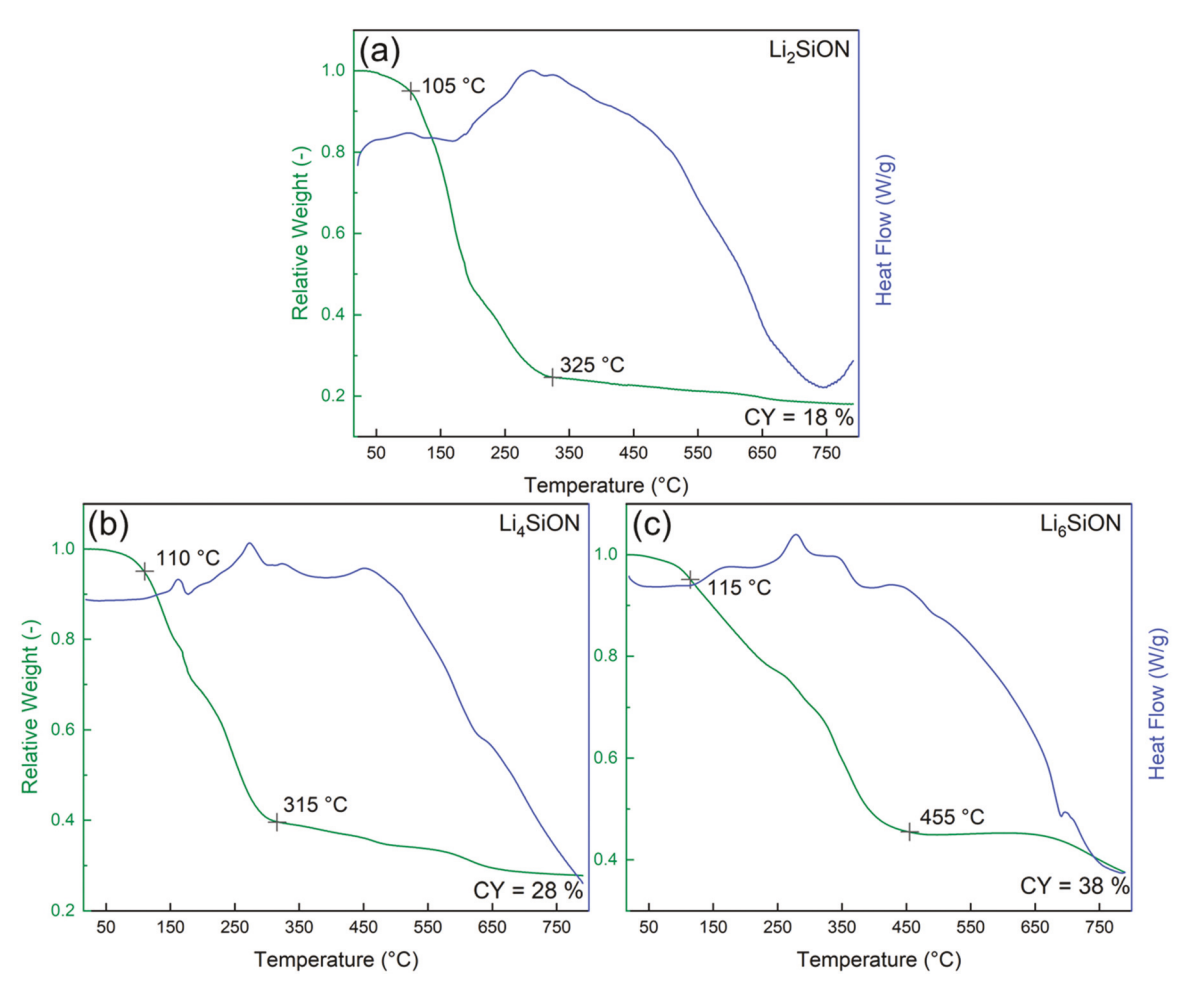


Fig. 6 TGA-DTAs (800 °C/10 °C min<sup>-1</sup>/N<sub>2</sub>) of Li<sub>2</sub>SiON (a), Li<sub>4</sub>SiON (b) and Li<sub>6</sub>SiON (c) precursors dried at 60 °C/1 h/vacuum.

 $\text{Li}_x \text{SiON}$  precursors show a broad peak at ~20°  $2\theta$  suggesting amorphous materials, indicating that SP reacts fully. As mentioned above, when dried at temperatures  $\leq 100$  °C,  $\text{Li}_x \text{SiON}$  precursors show similar XRD patterns, see Fig. S11b‡ comparing XRDs of  $\text{Li}_6 \text{SiON}$  dried at RT-100 °C/vacuum as an example. It's noteworthy that there is a small peak at 33°  $2\theta$  in the XRD corresponding to  $\text{Li}(\text{OH})(\text{H}_2\text{O})$ , likely due to brief interactions with atmospheric moisture during sample preparation, but the intensity is very low.

To study XRDs of Li<sub>x</sub>SiON precursors heated to higher temperatures (>100 °C), dried polymer precursor powders (60 °C/24 h/vacuum, 0.1–0.2 g) were compacted into pellets using a 13 mm diameter die at 10 ksi/RT (Fig. S3‡). The resulting pellets were heated between Al<sub>2</sub>O<sub>3</sub> disks to 100°–400 °C/2 h at 1 °C min<sup>-1</sup> under 120 ml min<sup>-1</sup> N<sub>2</sub> flow.

Fig. 7 presents XRD patterns of Li<sub>x</sub>SiON pellets heated to 100°–400°C/2 h/N<sub>2</sub>. The XRD of Li<sub>2</sub>SiON pellet (Fig. 7a) heated to 100 °C exhibits small peaks at ~20° and 30° 2 $\theta$ , corresponding to LiSi<sub>2</sub>N<sub>3</sub> (PDF-01-086-6830) with space group *Cmc*21. The pellet also exhibits a large broad peak from ~30° to 40° 2 $\theta$  with a central and shoulder peaks at 35° and 38° 2 $\theta$  associated with an amorphous phase. The small peak ~30° 2 $\theta$ 

disappears when the  $\rm Li_2SiON$  pellet is heated to 200°–300 °C. The broad peak seems to shift to lower diffraction angles (20°–30°  $\rm 2\theta$ ) when the pellet is heated to 400 °C.

Fig. 7b shows that  $\rm Li_4SiON$  pellets present a broad peak similar to  $\rm Li_2SiON$  after heating to 100 °C. No apparent sharp peaks appear on heating to 200°–300 °C confirming the absence of any ordered crystalline structure. At 400 °C, the amorphous peak shifts to lower diffraction angles with a shoulder peak at ~32° 2 $\theta$ , suggesting that the lattice is expanding. This might be ascribed to nitrogen loss which results in a change in composition and structure.

The XRD of Li<sub>6</sub>SiON pellets (Fig. 7c) at 100 °C is dominated by a broad peak corresponding to a poorly crystallized material, indicating an amorphous nature. The sharp peak at 35°  $2\theta$  can be indexed to partially crystalline Li<sub>4</sub>SiO<sub>4</sub> (PDF-01-084-7600) after heating to 200 °C. The single peak at ~22°  $2\theta$  starts to split into doublets when the Li<sub>6</sub>SiON pellet is heated above 300 °C. The doublets at ~30°  $2\theta$  for the pellet heated to 400 °C corresponds to Li<sub>2</sub>CO<sub>3</sub> (PDF-04-0101-7186). Since the Li<sub>6</sub>SiON precursor contains a relatively larger LiNH<sub>2</sub> component, it is quite likely to form Li<sub>2</sub>CO<sub>3</sub> during the decomposition process, which will generate CO<sub>2</sub>.

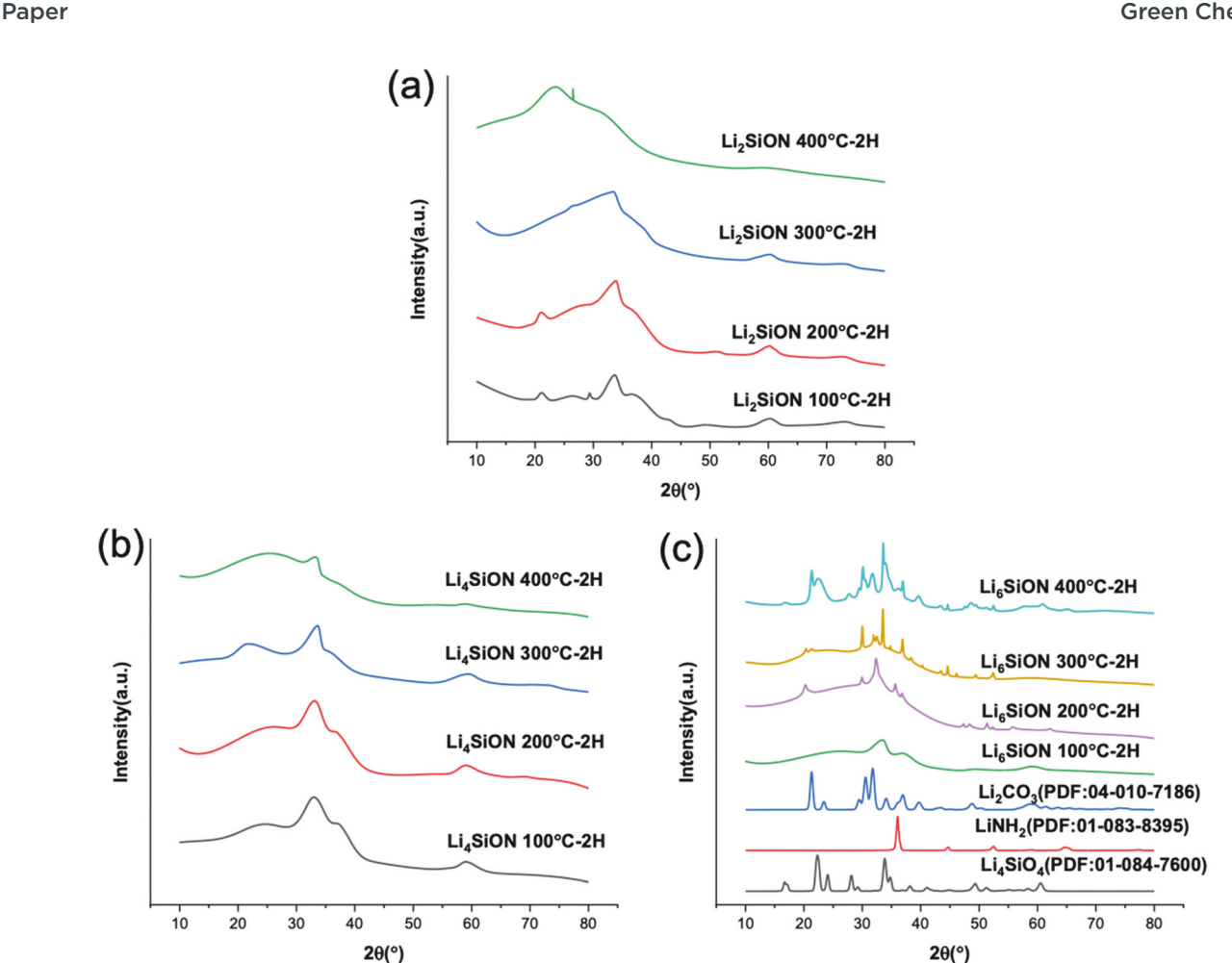


Fig. 7 XRDs of Li<sub>2</sub>SiON (a), Li<sub>4</sub>SiON (b), Li<sub>6</sub>SiON (c) pellets heated to 100°-400 °C/2 h/N<sub>2</sub>.

The amorphous nature of the Li<sub>x</sub>SiON precursors ≤100 °C by XRD fails to reveal elemental compositions of as-synthesized materials. Hence, LixSiON precursors (dried at ≤100 °C, powders) were characterized by XPS. For each sample, a wide-scan survey was done on three separate points for better accuracy. As shown in Fig. 8, all precursors show peaks for O, C and Li, small amounts of N and Si, and little difference is observed at different drying temperatures. SP, on the other hand, only shows peaks for O, C, and Si with higher intensity (Fig. S12‡).

Table 3 summarizes the average at% for Li<sub>x</sub>SiON precursors dried at different temperatures compared to SP. In general, Li<sub>x</sub>SiON precursors show lower C and Si contents compared to SP as expected, but the O content increases which may be LiOH and/or Li<sub>2</sub>CO<sub>3</sub> formed due to brief exposure in air.

The at.% for all LixSiON precursors stay nearly the same after drying at different temperatures under vacuum. The Li content increases with the amount of added LiNH2 as expected, but the increase from Li<sub>4</sub>SiON to Li<sub>6</sub>SiON is smaller than the increase from Li<sub>2</sub>SiON to Li<sub>4</sub>SiON, suggesting that Li content saturation is likely reached for the Li<sub>6</sub>SiON precursor. The fluxional nature of this one precursor belies the large excess of LiNH2 originally added and strongly suggests novel chemistry for this system since, we originally assumed that only two amide groups might be accommodated based on eqn (2). Unfortunately, this same fluxional nature means that NMR characterization was not possible at least at ambient.

For Li<sub>2</sub>SiON and Li<sub>4</sub>SiON precursors, C and Si contents decrease with increasing Li content, but the O content shows the opposite trend. As mentioned above, this is likely a result of LiOH and/or Li<sub>2</sub>CO<sub>3</sub> forming, and a higher Li content leads to a higher O content.

For the Li<sub>6</sub>SiON precursor, C and O contents are similar to the Li<sub>4</sub>SiON precursor, which may be related to the similar Li contents. However, after drying at 100 °C/1 h/vacuum, we can see a significant decrease in the C content and increases in the Li, O and Si contents. C may come from adsorbed organics during sample preparation that are volatile and removed on drying at a higher temperature resulting in increased percentages for the other elements.

However, the N content ranges between 0.7-0.9 at% for all precursors. Since all samples were kept under vacuum overnight prior to XPS scans (10<sup>-9</sup>-10<sup>-7</sup> Torr), -NH<sub>2</sub> is like eliminated as NH<sub>3</sub>, and the residual or "stable" N is similar for all

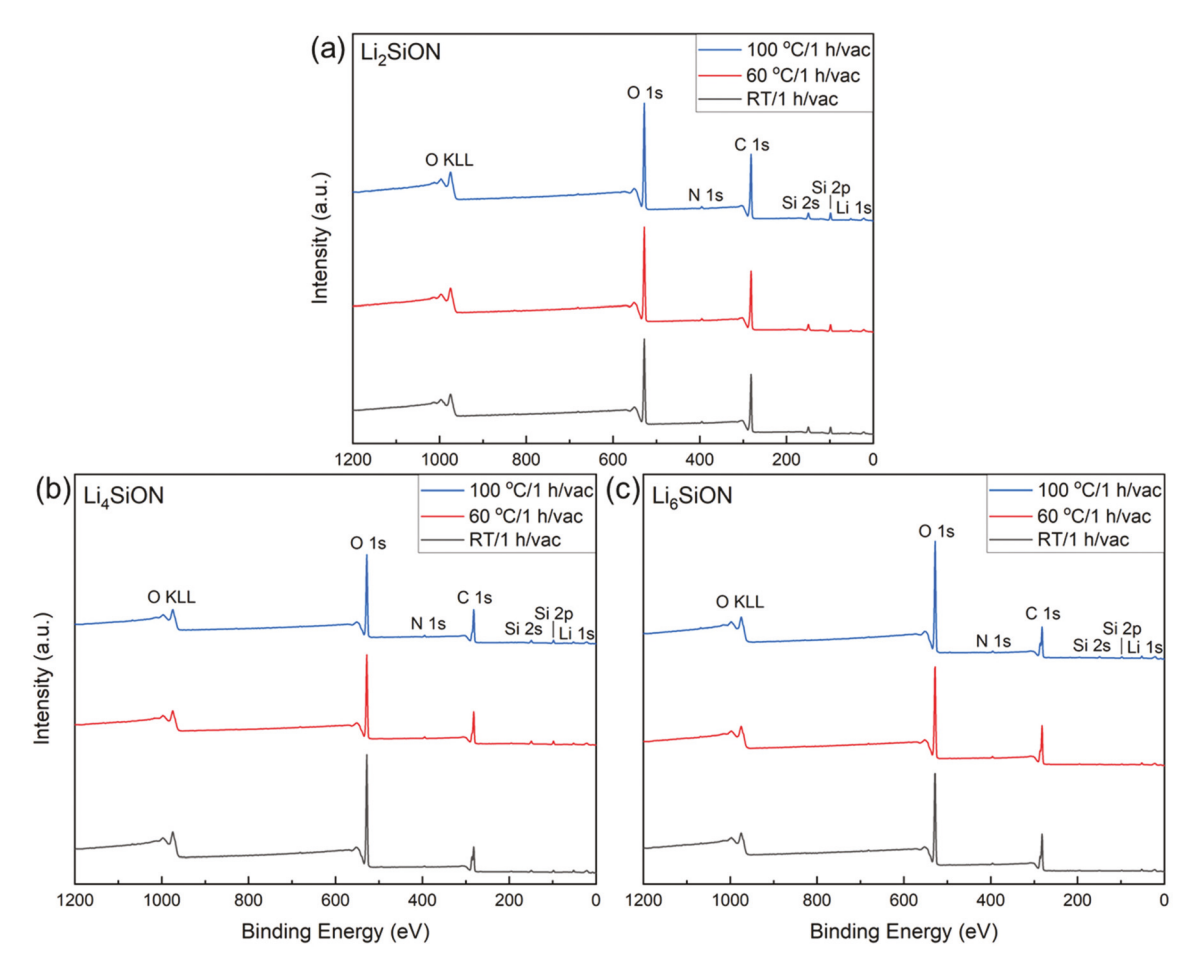


Fig. 8 Wide-scan survey XPS spectra of Li<sub>2</sub>SiON (a), Li<sub>4</sub>SiON (b) and Li<sub>6</sub>SiON (c) precursors dried at RT, 60° and 100 °C/1 h/vacuum respectively.

Table 3 Average atomic percentage (at%) of Li<sub>x</sub>SiON precursors dried at different temperatures in comparison with SP (60 °C/12 h/vacuum), analyzed by CasaXPS

°C/12 h/vacuum /1 h/vacuum	 13.0	80.0	_	14.1	5.0
/1 h/vacuum	12.0				5.0
	13.0	56.3	0.8	23.3	6.7
°C/1 h/vacuum	12.9	55.5	0.8	24.3	6.5
°C/1 h/vacuum	13.3	54.6	0.8	25.0	6.2
/1 h/vacuum	24.9	40.3	0.7	31.8	2.3
°C/1 h/vacuum	23.9	42.8	1.0	28.0	4.2
°C/1 h/vacuum	22.1	45.0	0.8	28.2	3.9
/1 h/vacuum	23.8	46.5	0.7	28.4	0.6
°C/1 h/vacuum	25.2	46.0	0.9	27.2	0.7
°C/1 h/vacuum	31.5	36.9	0.7	29.4	1.5
	0 °C/1 h/vacuum /1 h/vacuum °C/1 h/vacuum 0 °C/1 h/vacuum /1 h/vacuum °C/1 h/vacuum	0°C/1 h/vacuum 13.3 /1 h/vacuum 24.9 °C/1 h/vacuum 23.9 0°C/1 h/vacuum 22.1 /1 h/vacuum 23.8 °C/1 h/vacuum 25.2	0°C/1 h/vacuum     13.3     54.6       /1 h/vacuum     24.9     40.3       0°C/1 h/vacuum     23.9     42.8       0°C/1 h/vacuum     22.1     45.0       /1 h/vacuum     23.8     46.5       0°C/1 h/vacuum     25.2     46.0	0°C/1 h/vacuum     13.3     54.6     0.8       /1 h/vacuum     24.9     40.3     0.7       °C/1 h/vacuum     23.9     42.8     1.0       0°C/1 h/vacuum     22.1     45.0     0.8       /1 h/vacuum     23.8     46.5     0.7       °C/1 h/vacuum     25.2     46.0     0.9	0°C/1 h/vacuum     13.3     54.6     0.8     25.0       /1 h/vacuum     24.9     40.3     0.7     31.8       °C/1 h/vacuum     23.9     42.8     1.0     28.0       0°C/1 h/vacuum     22.1     45.0     0.8     28.2       /1 h/vacuum     23.8     46.5     0.7     28.4       °C/1 h/vacuum     25.2     46.0     0.9     27.2

precursors. In contrast, the MALDI studies on LixSiON solution droplets dried in vacuo for only a few minutes retained -NH2 groups presenting much higher N contents (~5-30 at% N excluding H) as suggested by composition calculations (Table 2). It is also worth mentioning that the at% analyzed by XPS may not be accurate as XPS only characterizes the sample surface to depths ≤10 nm.

Representative N 1s and Si 2p core-level XPS spectra of LixSiON precursors (dried at 60 °C/1 h/vacuum) are given in Fig. S13.‡ All LixSiON precursors show an N 1s peak at ~396-397 eV (Fig. S13a‡), which can be ascribed to Li-NH from LiNH2. Due to the low N content, the N 1s intensity is relatively low for all precursors. It is noticeable that the N 1s peak shifts to lower binding energy (BE) as the Li content increases, i.e., BE of the N 1s peak (BE<sub>N</sub>) follows Li<sub>2</sub>SiON >  $\text{Li}_4\text{SiON} > \text{Li}_6\text{SiON}$ , with a  $\Delta_{\text{BE}}$  of 0.4–0.5 eV. Since the BE is related to electron density, as the electronegativity (EN) of surrounding atoms decreases, electron density increases for the base element and BE decreases. For LixSiON precursors, as the Li (low EN) content increases, Li<sup>+</sup> concentration increases but the "stable" N content stays at ~1 at% for all precursors (Table 3), resulting in increased electron density around N and thus lower BE.

For Si 2p XPS spectra, all Li<sub>x</sub>SiON precursors exhibit Si 2p<sub>1/2</sub> and  $2p_{3/2}$  peaks ascribed to Si-O from SP. Similar to N 1s peaks, the Si 2p peak shifts to lower BE as the Li content increases (BEsi: SP > Li2SiON > Li4SiON > Li6SiON), which is likely due to the increased number of Li<sup>+</sup> that interact with the O from SP as suggested by NMR studies.

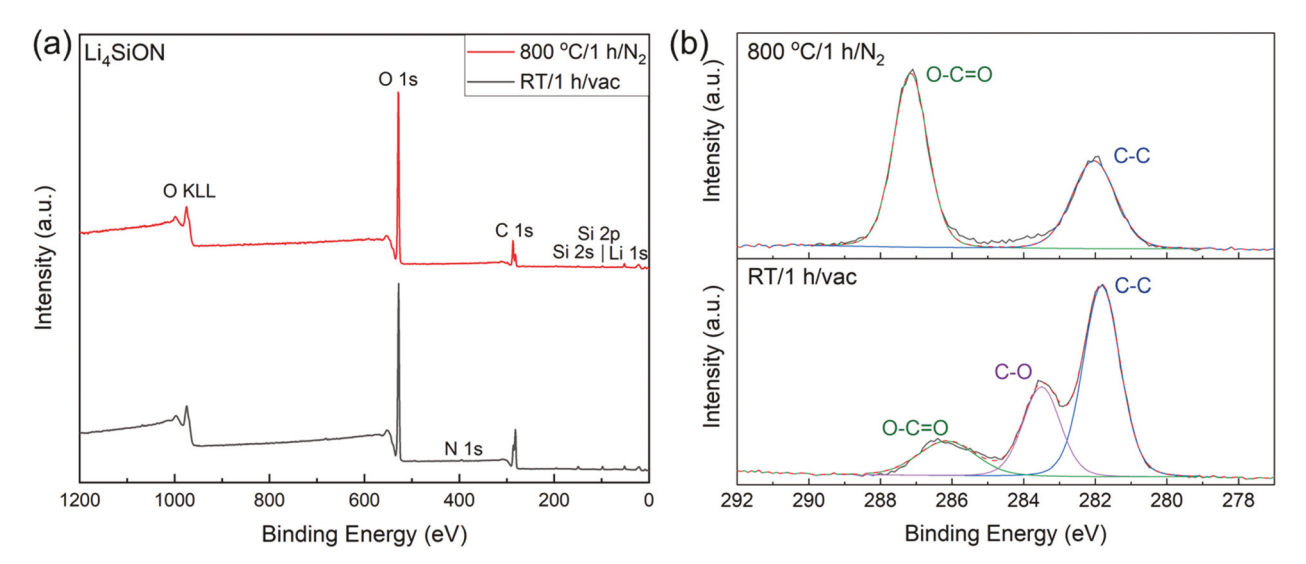


Fig. 9 (a) Wide-scan survey XPS spectra of Li<sub>4</sub>SiON treated at RT/1 h/vacuum and 800 °C/1 h/N<sub>2</sub>. (b) C 1s core-level spectra of Li<sub>4</sub>SiON treated at RT/1 h/vacuum and 800 °C/1 h/N<sub>2</sub>.

Table 4 XPS analyses (by CasaXPS) of the Li<sub>4</sub>SiON precursor treated at different temperatures

	Condition	Li 1s	C 1s	N 1s	O 1s	Si 2p
Binding energy (eV)	RT/1 h/vacuum	52	282, 284, 286	396	529	99
	800 °C/1 h/N <sub>2</sub>	52	282, 287	_	529	98
Average at%	RT/1 h/vacuum	24.9	40.3	0.7	31.8	2.3
o .	800 °C/1 h/N $_2$	36.6	25.3	_	37.0	1.2

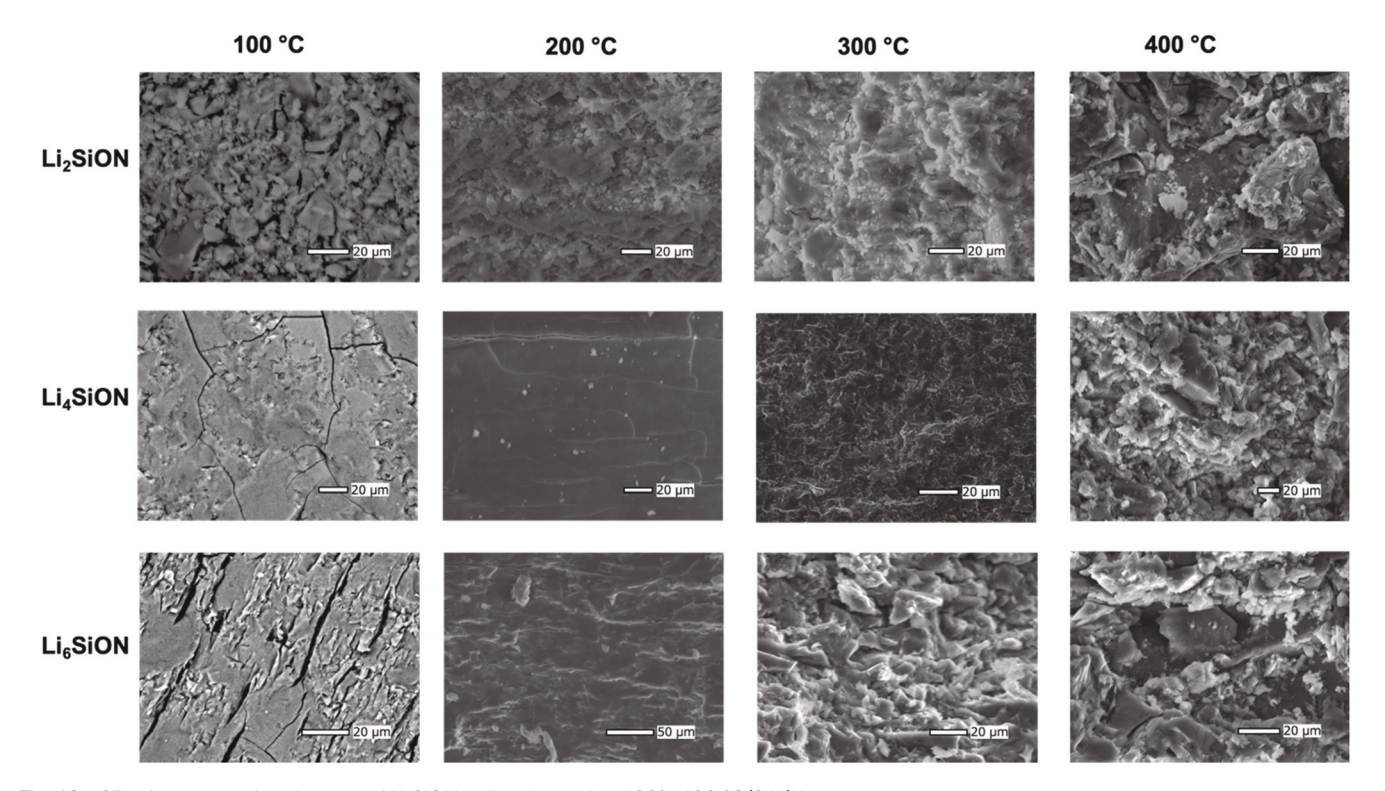


Fig. 10 SEM fracture surface images of  $Li_x$ SiON pellets heated to 100°-400 °C/2 h/N<sub>2</sub>.

To study high temperature compositions of Li<sub>r</sub>SiON precursors, precursor pellets (Fig. S3<sup>‡</sup>) were heated to 800 °C/1 h/N<sub>2</sub> in a tube furnace and characterized by FTIR, XRD and XPS. Fig. S14a‡ compares the FTIRs of Li<sub>x</sub>SiON heated to 800 °C/ 1 h/N<sub>2</sub>. Peaks at ~1450 cm<sup>-1</sup> are present for all precursors, which may be carbonate and/or silicate peaks. The peaks at  $\sim 1000-800 \text{ cm}^{-1}$  are likely  $\nu \text{Si-O}$  ( $\sim 1050 \text{ cm}^{-1}$ ) and possibly some  $\nu$ Si-N (960-840 cm<sup>-1</sup>), <sup>78-82</sup> or silicate peaks.

Fig. S14b‡ compares the XRDs of Li<sub>4</sub>SiON (800 °C/1 h/N<sub>2</sub>) and Li<sub>4</sub>SiO<sub>4</sub> as an example. Both the pellets and ground powder show the same diffraction peaks, suggesting phase uniformity of the bulk surface and interior. These peaks fit well with monoclinic Li<sub>4</sub>SiO<sub>4</sub>, in agreement with FTIR analyses in Fig. S14a.‡

Fig. 9a compares the XPS spectra of Li<sub>4</sub>SiON treated at RT/ 1 h/vacuum and 800 °C/1 h/N2. Both spectra show the same main peaks for O, C, Si and Li. Only trace amounts of N are found in Li<sub>4</sub>SiON treated at RT/1 h/vacuum, and no N in Li<sub>4</sub>SiON treated at 800 °C/1 h/N<sub>2</sub>.

Table 4 summarizes the XPS analyses of Li<sub>4</sub>SiON treated at different temperatures. Li and O contents increase after heating to 800 °C while C and N contents decrease due to decomposition of organic groups.

As for the binding energy, all elements remain mostly the same after heating to 800 °C except for C per Table 4. Fig. 9b compares C 1s core-level spectra of Li<sub>4</sub>SiON treated at RT/1 h/ vacuum and 800 °C/1 h/N<sub>2</sub>. The as-synthesized Li<sub>4</sub>SiON (RT/ 1 h/vacuum) show three different C 1s peaks, corresponding to O-C=O from carbonate, and C-O and C-C from SP. After heating to 800 °C, as the organic components decompose, C-O disappears and the intensity of C-C drops (residual carbon), leaving a large carbonate peak (O-C=O) that also corresponds to the band at ~1450 cm<sup>-1</sup> in the FTIR (Fig. S14a‡). Overall, after heating to 800 °C/1 h/N<sub>2</sub>, the precursors form stable crystalline Li<sub>4</sub>SiO<sub>4</sub> and small amounts of Li<sub>2</sub>CO<sub>3</sub>.

To further characterize the composition and microstructures of the Li<sub>x</sub>SiON precursors, SEM and EDX were conducted on precursor pellets (Fig. S3‡), respectively.

Fig. 10 shows SEM fracture surface images of Li<sub>2</sub>SiON, Li<sub>4</sub>SiON, and Li<sub>6</sub>SiON precursor pellets heated to 100°-400 °C/ 2 h/N<sub>2</sub>. The Li<sub>4</sub>SiON and Li<sub>6</sub>SiON pellets heated between 100°-200 °C, in general, showed a smooth, uniform, and dense microstructure, typical for polymeric materials. This can be ascribed to the fact that these precursors relatively show a small mass loss (20 wt%) before 250 °C. The densification at 200 °C for the Li<sub>4</sub>SiON and Li<sub>6</sub>SiON pellets might be a result of

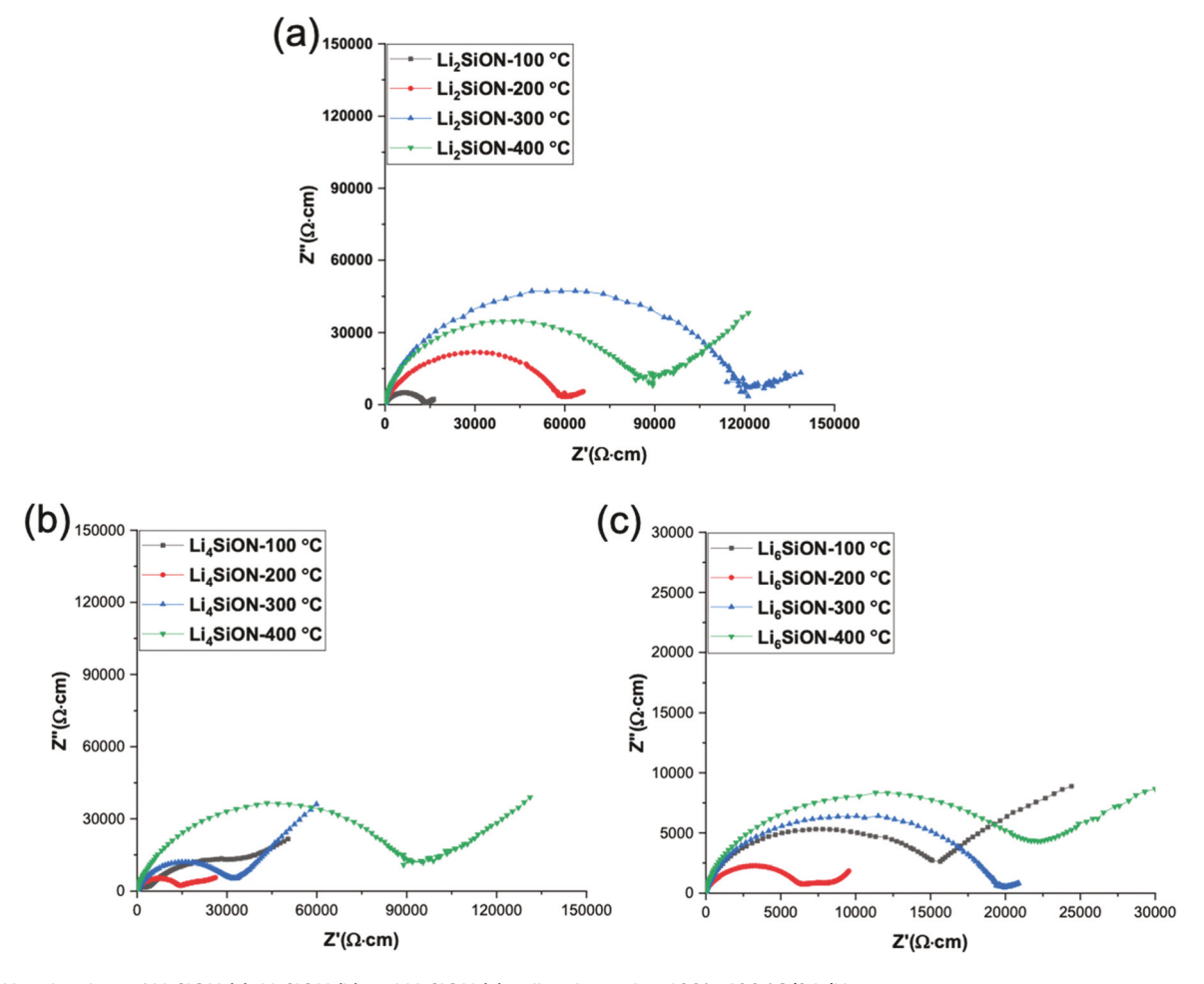


Fig. 11 Nyquist plots of Li<sub>2</sub>SiON (a), Li<sub>4</sub>SiON (b) and Li<sub>6</sub>SiON (c) pellets heated to 100°-400 °C/2 h/N<sub>2</sub>.

rearrangement between the polymeric chains during heat treatment; it may be also associated with a phase change as suggested by XRD for Li<sub>6</sub>SiON (Fig. 7c). In comparison to pellets with high Li content, the microstructure of Li<sub>2</sub>SiON pellet reveals porous structures on heating between  $100^{\circ}$ –200 °C, attributed to the large mass loss (50 wt%) before 250 °C (Fig. 6a).

The pellets heated between 300°-400 °C exhibit crystalline features with uneven fracture surface (grain boundary fractures) as well as micropores associated with the loss of volatile and organic compounds and ceramization of the precursors.

Table S3‡ lists densities of Li<sub>x</sub>SiON precursor pellets treated under different conditions. The as-synthesized precursors (dried at 60 °C/1 h/vacuum) show densities close to 1 g cm<sup>-3</sup>, which is typical for polymeric materials. After heat treatment to  $100^{\circ}$ –400 °C/2 h/N<sub>2</sub>, all precursors show increased densities, which may be arised from polymeric structural rearrangements, and ceramization at higher temperatures (≥300 °C, Fig. 10). In general, the density increases with temperature, but Li<sub>2</sub>SiON and Li<sub>4</sub>SiON precursors show decreased density when the temperature increased from 300° to 400 °C, likely due to decomposition of organic compounds, consistent with SEM (Fig. 10) and TGA-DTA studies (Fig. 6). The Li<sub>6</sub>SiON precursor shows better thermal stability as suggested by TGA-DTA (Fig. 6), therefore its density increases after heating to 400 °C.

Fig. S15-S17‡ show EDX map images of  $Li_x$ SiON pellets heated to  $100^{\circ}$ - $400 \,^{\circ}$ C/2 h/N<sub>2</sub>. The EDX map of pellets heated

Table 5 Total conductivities ( $\sigma_{RT}$ ) of Li $_x$ SiON pellets heated to 100°-400 °C/2 h/N $_2$ 

Precursor pellet	Temp. (°C)	$\sigma_{\mathrm{RT}} \left( \mathrm{S \ cm}^{-1} \right)$
Li <sub>2</sub> SiON	100/2 h	$7.4 \times 10^{-7}$
2	200/2 h	$2.5 \times 10^{-7}$
	300/2 h	$1.4 \times 10^{-8}$
	400/2 h	$2.0 \times 10^{-8}$
Li <sub>4</sub> SiON	100/2 h	$2.3 \times 10^{-7}$
•	200/2 h	$9.0 \times 10^{-7}$
	300/2 h	$4.6 \times 10^{-7}$
	400/2 h	$1.1 \times 10^{-7}$
Li <sub>6</sub> SiON	100/2 h	$5.8 \times 10^{-6}$
0	200/2 h	$8.5 \times 10^{-6}$
	300/2 h	$4.3 \times 10^{-6}$
	400/2 h	$2.7 \times 10^{-6}$

to 100 °C shows well-distributed signature elements (N, O, and Si) as well as C from the starting material (SP) in good agreement with XPS per Fig. 8 and Table 3. Quantitative EDX results are summarized in Table S4.‡ In general, the N content decreases with increasing temperature. This is likely due to loss of  $-NH_2$  (Table 3). In addition, the C content also decreases as pellets are heated to 400 °C, also ascribed to decomposition of volatile and absorbed organic compounds (Fig. 6).

#### 3.2. Ionic conductivity measurements

Fig. 11a–c shows Nyquist plots of  $\text{Li}_2\text{SiON}$ ,  $\text{Li}_4\text{SiON}$ , and  $\text{Li}_6\text{SiON}$  pellets heated to  $100^\circ$ –400 °C/2 h/N<sub>2</sub>, respectively. All the measurements were conducted at room temperature. Detailed experimental procedures for ionic impedance measurements are provided in the ESI.‡

Table 5 summarizes total conductivities of the polymer precursor pellets heated to  $100^{\circ}$ – $400^{\circ}$ C/2 h/N<sub>2</sub>. The Li<sub>2</sub>SiON pellet showed the highest conductivity when heated to  $100^{\circ}$ C as shown in Fig. 11a.‡ The total conductivities decrease with increasing temperature to 300 °C, likely as a result of N loss per EDX in Fig. S15.‡ The slight increase in ionic conductivity at  $400^{\circ}$ C for the Li<sub>2</sub>SiON pellet might be a consequence of lower C contents. There seems to be a tradeoff between the loss of N and decreases in C content when the pellets are heated to higher temperatures (*i.e.* >300 °C) per Table S4.‡ The decrease in C content is desirable as it decreases the electronic conductivity of the electrolyte.

 ${\rm Li_4SiON}$  and  ${\rm Li_6SiON}$  pellets show the highest conductivities of  $9\times 10^{-7}$  and  $8.5\times 10^{-6}~{\rm S~cm^{-1}}$  at 200 °C, respectively. The increase in conductivity is associated with the denser microstructures of both precursors at 200 °C, Fig. 10. The total resistivity increases on heating to 300°–400 °C, a likely result of the decrease in N contents.

Table 6 compares the ionic conductivities of  $\text{Li}_4 \text{SiO}_4$  and LiSiON systems with different synthesis/processing methods in literature. Reported  $\text{Li}_4 \text{SiO}_4$  conductivities are typically measured at elevated temperatures (>100 °C). In general,  $\text{Li}_4 \text{SiO}_4$  sintered from sol–gel processed nanopowders show higher conductivities compared to  $\text{Li}_4 \text{SiO}_4$  prepared via solid-state reaction. Adnan *et al.*<sup>53</sup> reported a high ambient bulk conductivity of  $\sim 3 \times 10^{-6} \text{ S cm}^{-1}$  for  $\text{Li}_4 \text{SiO}_4$  by sol–gel processing and sintering at 750 °C/4 h, which is still lower than the

Table 6 Comparison of ionic conductivities (σ) of Li<sub>4</sub>SiO<sub>4</sub> and LiSiON systems with different synthesis/processing methods in the literature

Composition/phase	Synthesis/processing method	$\sigma$ (S cm <sup>-1</sup> ) at $T$ °C	Thickness <sup>a</sup> (mm)	Ref.
Li <sub>4</sub> SiO <sub>4</sub> (monoclinic)	Sol–gel and sintering (1000 °C/4 h)	$\sim 10^{-5} (250)$	~2	51
Li <sub>4</sub> SiO <sub>4</sub> (monoclinic)	Sol-gel and sintering (750 °C/4 h)	$\sim 3 \times 10^{-6} \text{ (RT)}; \sim 10^{-4} \text{ (100)}$	_	53
Li <sub>4</sub> SiO <sub>4</sub> (monoclinic)	Solid state reaction (1000–1050 °C/18–24 h)	$\sim 10^{-7} (150)$	_	55 and 57
Li <sub>4</sub> SiO <sub>4</sub> (monoclinic)	Solid state reaction (1200 °C/10 h)	$2.5 \times 10^{-6} (300)$	_	59
30Si <sub>2</sub> O·61SiO <sub>2</sub> ·3Si <sub>3</sub> N <sub>4</sub> (LiSiON glass)	Melt mixing (1400–1450 °C/N <sub>2</sub> )	$2.5 \times 10^{-8} (40)$	~1	50
Li <sub>6</sub> SiON (amorphous)	Polymer precursor synthesis and heating to	$8.5 \times 10^{-6}  (RT)$	0.2-0.3	This work
· - /	200 °C/2 h	• /		

<sup>&</sup>lt;sup>a</sup> All conductivities are measured on pellets; thicknesses are not provided in some work.

highest ambient conductivity of  $8.5 \times 10^{-6}~S~cm^{-1}$  for Li<sub>6</sub>SiON heated to 200 °C/2 h. For N-doped systems, the only LiSiON glass ionic conductivity measurement found in the literature records a low value of  $2.5 \times 10^{-8}$  at 40~°C. <sup>50</sup>

Furthermore, compared to other synthesis and processing methods listed in Table 6, the polymer precursor synthesis is easily scalable; dense microstructures (Fig. 10) and optimum conductivities (Table 5) are obtained for  $\text{Li}_x \text{SiON}$  (x = 4, 6) pellets when heated only to 200 °C/2 h/N<sub>2</sub>, which significantly reduces processing steps, temperatures, and cost.

#### 4. Conclusions

In summary, we present here the green synthesis and detailed characterization of Li<sub>r</sub>SiON oligomer/polymer precursors, including FTIR, MALDI-ToF, NMR, TGA-DTA, XRD, XPS, EDX, SEM and impedance studies. XPS shows that the Li content increases with LiNH2 amounts, which also correlates with MWs and CYs. <sup>7</sup>Li NMR suggests that Li<sup>+</sup> ions are well solvated and dissociated, and excess Li+ may exist in clusters, which is beneficial for their electrochemical performances. When x = 6, the Li content reaches a saturation level suggested by XPS; <sup>1</sup>H, <sup>13</sup>C and <sup>29</sup>Si NMRs indicate fluxional motion. Li<sub>x</sub>SiON precursors start to decompose at ~100 °C due to organic portions. When dried at ≤100 °C, XRD patterns show an amorphous phase; when heated to 800 °C, Li<sub>4</sub>SiO<sub>4</sub> forms, suggesting a polymer to ceramic conversion at higher temperatures. SEM and impedance studies show that dense microstructures and optimum conductivities are obtained after heating to 200 °C/ 2 h/N<sub>2</sub> for Li<sub>x</sub>SiON (x = 4, 6) pellets. In general, conductivities of precursor pellets increase with Li content: Li<sub>6</sub>SiON > Li<sub>4</sub>SiON > Li<sub>2</sub>SiON.

Future work will demonstrate the utility of these precursors, especially  $\text{Li}_6\text{SiON}$  when used in symmetric cells and half cells, impregnated in Celgard, or as solid solutions with poly (ethylene oxide) (PEO).

#### Conflicts of interest

There are no conflicts to declare.

### Acknowledgements

We are grateful for the support of a significant portion of this work by DMR NSF Grant No. DMR-1926199 and a gift from Mercedes Benz Research and Development North America (MBRDNA). A portion of the work was also supported by University of Michigan Rackham Merit fellowship. We also acknowledge the financial support of the University of Michigan College of Engineering and NSF grant no. DMR-0402785, and technical support from the Michigan Center for Materials Characterization. We especially thank Mr Andrew Alexander for his assistance in developing the computer program for polymer precursor composition calculations

based on MALDI-ToF. We also thank Zejun Sun, Tianle Liu, and Mengjie Yu for their help in synthesizing SP. We also would like to thank Wadham Energy LP for providing the RHA powders.

#### References

- 1 C. Yuan, H. B. Wu, Y. Xie and X. W. Lou, *Angew. Chem., Int. Ed.*, 2014, 53, 1488–1504.
- 2 S. B. Peterson and J. J. Michalek, *Energy Policy*, 2013, 52, 429–438.
- 3 L. L. Gaines and J. B. Dunn, in *Lithium-Ion Batteries*, ed. G. Pistoia, Elsevier, Amsterdam, 2014, pp. 483–508.
- 4 T. Jiang, P. He, G. Wang, Y. Shen, C.-W. Nan and L.-Z. Fan, *Adv. Energy Mater.*, 2020, **10**, 1903376.
- 5 A. Manthiram, X. Yu and S. Wang, *Nat. Rev. Mater.*, 2017, 2, 1–16.
- 6 J. W. Fergus, J. Power Sources, 2010, 195, 4554-4569.
- 7 K. Xu, Chem. Rev., 2004, 104, 4303-4418.
- 8 X.-B. Cheng, R. Zhang, C.-Z. Zhao, F. Wei, J.-G. Zhang and Q. Zhang, *Adv. Sci.*, 2016, 3, 1500213.
- 9 C. S. Nimisha, K. Y. Rao, G. Venkatesh, G. M. Rao and N. Munichandraiah, *Thin Solid Films*, 2011, **519**, 3401–3406.
- 10 X. Yu, J. B. Bates, G. E. Jellison and F. X. Hart, J. Electrochem. Soc., 1997, 144, 524–532.
- 11 J. B. Bates, N. J. Dudney, G. R. Gruzalski, R. A. Zuhr, A. Choudhury, C. F. Luck and J. D. Robertson, *J. Power Sources*, 1993, 43–44, 103–110.
- 12 A. Reyes Jiménez, R. Nölle, R. Wagner, J. Hüsker, M. Kolek, R. Schmuch, M. Winter and T. Placke, *Nanoscale*, 2018, 10, 2128–2137.
- 13 Z. Hu, D. Li and K. Xie, Bull. Mater. Sci., 2008, 31, 681-686.
- 14 S. J. Lee, J. H. Bae, H. W. Lee, H. K. Baik and S. M. Lee, *J. Power Sources*, 2003, **123**, 61–64.
- 15 F. Muñoz, A. Durán, L. Pascual, L. Montagne, B. Revel and A. C. M. Rodrigues, *Solid State Ionics*, 2008, **179**, 574–579.
- 16 P. E. Stallworth, F. Vereda, S. G. Greenbaum, T. E. Haas, P. Zerigian and R. B. Goldner, *J. Electrochem. Soc.*, 2005, 152, A516–A522.
- 17 B. Fleutot, B. Pecquenard, H. Martinez, M. Letellier and A. Levasseur, *Solid State Ionics*, 2011, **186**, 29–36.
- 18 N. Mascaraque, J. L. G. Fierro, A. Durán and F. Muñoz, Solid State Ionics, 2013, 233, 73-79.
- 19 J. B. Bates, N. J. Dudney, G. R. Gruzalski, R. A. Zuhr, A. Choudhury, C. F. Luck and J. D. Robertson, *Solid State Ionics*, 1992, 53, 647–654.
- 20 B. Wang, B. S. Kwak, B. C. Sales and J. B. Bates, *J. Non-Cryst. Solids*, 1995, 183, 297–306.
- 21 B. Put, P. M. Vereecken, J. Meersschaut, A. Sepúlveda and A. Stesmans, *ACS Appl. Mater. Interfaces*, 2016, **8**, 7060–7069
- 22 Y. Hamon, A. Douard, F. Sabary, C. Marcel, P. Vinatier, B. Pecquenard and A. Levasseur, *Solid State Ionics*, 2006, 177, 257–261.

Paper

- 23 S. Zhao, Z. Fu and Q. Qin, *Thin Solid Films*, 2002, **415**, 108–113
- 24 W. Y. Liu, Z. W. Fu, C. L. Li and Q. Z. Qin, *Electrochem. Solid-State Lett.*, 2004, 7, J36–J40.
- 25 F. Vereda, R. B. Goldner, T. E. Haas and P. Zerigian, *Electrochem. Solid-State Lett.*, 2002, 5, 239–241.
- 26 Y. G. Kim and H. N. G. Wadley, J. Vac. Sci. Technol., A, 2008, 26, 174–183.
- 27 S. Nowak, F. Berkemeier and G. Schmitz, *J. Power Sources*, 2015, 275, 144–150.
- 28 H. T. Kim, T. Mun, C. Park, S. W. Jin and H. Y. Park, I. Power Sources, 2013, 244, 641–645.
- 29 F. Xu, N. J. Dudney, G. M. Veith, Y. Kim, C. Erdonmez, W. Lai and Y. M. Chiang, J. Mater. Res., 2010, 25, 1507– 1515.
- 30 A. C. Kozen, A. J. Pearse, C. F. Lin, M. Noked and G. W. Rubloff, *Chem. Mater.*, 2015, 27, 5324–5331.
- 31 B. Wang, B. C. Chakoumakos, B. C. Sales, B. S. Kwak and J. B. Bates, *J. Solid State Chem.*, 1995, 115, 313–323.
- 32 N. S. Roh, S. D. Lee and H. S. Kwon, *Scr. Mater.*, 1999, **42**, 43–49.
- 33 L. Meda and E. E. Maxie, *Thin Solid Films*, 2012, **520**, 1799–1803.
- 34 L. Le Van-Jodin, F. Ducroquet, F. Sabary and I. Chevalier, *Solid State Ionics*, 2013, **253**, 151–156.
- 35 Y. Su, J. Falgenhauer, A. Polity, T. Leichtweiß, A. Kronenberger, J. Obel, S. Zhou, D. Schlettwein, J. Janek and B. K. Meyer, *Solid State Ionics*, 2015, **282**, 63–69.
- 36 P. Birke, W. F. Chu and W. Weppner, *Solid State Ionics*, 1996, 93, 1–15.
- 37 P. Birke and W. Weppner, *Electrochim. Acta*, 1997, **42**, 3375–3384.
- 38 Y. Hamon, P. Vinatier, E. I. Kamitsos, M. Dussauze, C. P. E. Varsamis, D. Zielniok, C. Roesser and B. Roling, *Solid State Ionics*, 2008, **179**, 1223–1226.
- 39 M. Dussauze, E. I. Kamitsos, P. Johansson, A. Matic, C. P. E. Varsamis, D. Cavagnat, P. Vinatier and Y. Hamon, J. Phys. Chem. C, 2013, 117, 7202–7213.
- 40 K. H. Joo, H. J. Sohn, P. Vinatier, B. Pecquenard and A. Levasseur, *Electrochem. Solid-State Lett.*, 2004, 7, 256–259.
- 41 W. Yang, W. Yang, B. Sun, S. Di, K. Yan, G. Wang and G. Shao, *ACS Appl. Mater. Interfaces*, 2018, **10**, 39695–39704.
- 42 B. Dong, R. Jarkaneh, S. Hull, N. Reeves-McLaren, J. J. Biendicho and A. R. West, J. Mater. Chem. A, 2015, 4, 1408–1413.
- 43 R. Jarkaneh, Novel Oxynitride Lithium Ion Conductors, 2015.
- 44 H. Unuma, J. Am. Ceram. Soc., 1993, 76, 1308-1312.
- 45 H. Unuma, T. Kokubo and S. Sakka, *J. Mater. Sci.*, 1988, 23, 4399–4405.
- 46 N. A. Wójcik, B. Jonson, D. Möncke, E. I. Kamitsos, H. Segawa, J. Karczewski and S. Ali, J. Non-Cryst. Solids, 2019, 522, 119585.
- 47 S. Sakka, J. Non-Cryst. Solids, 1995, 181, 215-224.
- 48 H. Unuma, Y. Suzuki, T. Furusaki, Y. Ishizuka and K. Kodaira, *J. Ceram. Soc. Jpn.*, 1989, **97**, 376–379.

- 49 H. Unuma and S. Sakka, J. Mater. Sci. Lett., 1987, 6, 996-998.
- 50 H. Unuma, K. Komori and S. Sakka, *J. Non-Cryst. Solids*, 1987, **95**, 913–920.
- 51 X. Wu, Z. Wen, X. Xu, X. Wang and J. Lin, *J. Nucl. Mater.*, 2009, **392**, 471–475.
- 52 X. Wu, Z. Wen, X. Xu and Y. Liu, Fusion Eng. Des., 2010, 85, 222–226.
- 53 S. B. R. S. Adnan, N. S. Mohamed and K. A. Norwati, Int. J. Eng. Math. Phys. Sci., 2011, 5, 183–186.
- 54 A. R. West, J. Appl. Electrochem., 1973, 3, 327-335.
- 55 A. Khorassani and A. R. West, J. Solid State Chem., 1984, 53, 369–375.
- 56 Y. Tao, D. Yi and J. Li, *Solid State Ionics*, 2008, **179**, 2396–2398.
- 57 A. Khorassani and A. R. West, *Solid State Ionics*, 1982, 7, 1–8
- 58 Y. Sakurai, A. Sakuda, A. Hayashi and M. Tatsumisago, *Solid State Ionics*, 2011, **182**, 59–63.
- 59 Y. Deng, C. Eames, J. N. Chotard, F. Laleire, V. Seznec, S. Emge, O. Pecher, C. P. Grey, C. Masquelier and M. S. Islam, J. Am. Chem. Soc., 2015, 137, 9136–9145.
- 60 K. Hirai, M. Tatsumisago and T. Minami, *Solid State Ionics*, 1995, **78**, 269–273.
- 61 Y. Kawakami, H. Ikuta, T. Uchida and M. Wakihara, *Thermochim. Acta*, 1997, **299**, 7–12.
- 62 H. Morimoto, H. Yamashita, M. Tatsumisago and T. Minami, *J. Ceram. Soc. Jpn.*, 2000, **108**, 128–131.
- 63 M. Tatsumisago, H. Morimoto, H. Yamashita and T. Minami, *Solid State Ionics*, 2000, **136–137**, 483–488.
- 64 Y. Ikeda, T. Kitade, S. Kohjiya, A. Hayashi, A. Matsuda, M. Tatsumisago and T. Minami, *Polymer*, 2001, **42**, 7225–7228.
- 65 X. Zhang, E. Temeche and R. M. Laine, *Macromolecules*, 2020, 53, 2702–2712.
- 66 E. Temeche, X. Zhang and R. M. Laine, *ACS Appl. Mater. Interfaces*, 2020, **12**, 20548–20562.
- 67 E. Temeche, X. Zhang and R. M. Laine, *ACS Appl. Mater. Interfaces*, 2020, **12**, 30353–30364.
- 68 E. Temeche, M. Yu and R. M. Laine, *Green Chem.*, 2020, 22, 4656–4668.
- 69 J. C. Marchal, D. J. Krug, P. McDonnell, K. Sun and R. M. Laine, *Green Chem.*, 2015, 17, 3931–3940.
- 70 R. M. Laine, J. C. Furgal, P. Doan, D. Pan, V. Popova and X. Zhang, *Angew. Chem., Int. Ed.*, 2016, 55, 1065–1069.
- 71 J. C. Furgal and R. M. Laine, *Bull. Chem. Soc. Jpn.*, 2016, **89**, 705–725.
- 72 M. L. Hoppe, R. M. Laine, J. Kampf, M. S. Gordon and L. W. Burggraf, *Angew. Chem., Int. Ed. Engl.*, 1993, 32, 287-
- 73 F. A. Cotton, Acc. Chem. Res., 1968, 1, 257-265.
- 74 P. I. Arvidsson, P. Ahlberg and G. Hilmersson, *Chem. Eur. J.*, 1999, **5**, 1348–1354.
- 75 K. K. Lee, K. Park, H. Lee, Y. Noh, D. Kossowska, K. Kwak and M. Cho, *Nat. Commun.*, 2017, **8**, 1–9.

- 76 K. A. See, M. Leskes, J. M. Griffin, S. Britto, P. D. Matthews, A. Emly, A. Van Der Ven, D. S. Wright, A. J. Morris, C. P. Grey and R. Seshadri, J. Am. Chem. Soc., 2014, 136, 16368–16377.
- 77 J. Zhang and Y. H. Hu, *Ind. Eng. Chem. Res.*, 2011, **50**, 8058–8064.
- 78 G. Scardera, T. Puzzer, G. Conibeer and M. A. Green, *J. Appl. Phys.*, 2008, **104**, 104310.
- 79 E. San Andrés, A. Del Prado, F. L. Martínez, I. Mártil, D. Bravo and F. J. López, *J. Appl. Phys.*, 2000, 87, 1187–1192.
- 80 J. A. Diniz, P. J. Tatsch and M. A. A. Pudenzi, *Appl. Phys. Lett.*, 1996, **69**, 2214–2215.
- 81 H. Ono, T. Ikarashi, Y. Miura, E. Hasegawa, K. Ando and T. Kitano, *Appl. Phys. Lett.*, 1999, 74, 203–205.
- 82 J. Viard, E. Beche, D. Perarnau, R. Berjoan and J. Durand, *J. Eur. Ceram. Soc.*, 1997, 17, 2025–2028.